ChemPhysChem

Research Article
doi.org/10.1002/cphc.202300091

Chemistry Europe
European Chemical Societies Publishing

www.chemphyschem.org

One- and Two-Electron Reductions in MiniSOG and their Implication in Catalysis**

Oksana Azpitarte,[a, b] Ane Zudaire,[a, b] Jon Uranga,[c] Xabier Lopez,[a, b] Luca Salassa,[a, b, d] Elena Formoso,[b, e] and Elixabete Rezabal*[a, b]

The unconventional bioorthogonal catalytic activation of anticancer metal complexes by flavin and flavoproteins photocatalysis has been reported recently. The reactivity is based on a two-electron redox reaction of the photoactivated flavin. Furthermore, when it comes to flavoproteins, we recently reported that site mutagenesis can modulate and improve this catalytic activity in the mini Singlet Oxygen Generator protein (SOG). In this paper, we analyze the reductive half-reaction in different miniSOG environments by means of density functional theory. We report that the redox properties of flavin and the resulting reactivity of miniSOG is modulated by specific mutations, which is in line with the experimental results in the literature. This modulation can be attributed to the fundamental physicochemical properties of the system, specifically (i) the competition of single and double reduction of the flavin and (ii) the probability of electron transfer from the protein to the flavin. These factors are ultimately linked to the stability of flavin's electron-accepting orbitals in different coordination modes.

Introduction

Flavin-dependent enzymes are a vast family of proteins presenting a flavin cofactor (see Figure 1 for the general structure), which catalyze a remarkable array of chemical transformations, ranging from redox to photochemical reactions, and operating on different substrates, including small organic molecules, organometallic complexes, and nucleic acids. This versatility is accomplished, to a great extent, thanks to the tuneability of the flavin cofactor's physicochemical properties, by means of the interactions established with the protein.[1–3]

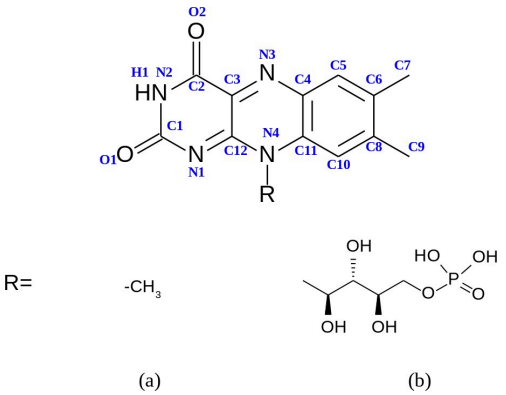

Figure 1. General chemical structure of flavin and the derivatives analyzed in this work: (a) lumiflavin (LF), and (b) flavin mononucleotide (FMN). In biological environments, the phosphoryl group of FMN is deprotonated, and therefore it has a double negative charge (FMN^{-2}).

In particular, the present work is focused on the mini singlet oxygen generator (miniSOG), which is a flavin mononucleotide (FMN)-containing flavoprotein, designed for $^1O_2$ sensitization purposes.[4–6] In the last years its catalytic activity has been extended to other, less common reactions, as the catalytic photoreduction of metal substrates[7–9] which are precursors of anticancer drugs such as cisplatin or carboplatin. This reactivity has two main steps (see Figure 2): the reductive half-reaction, in which [$^1FMN^{-2}$] is irradiated with low dose of visible-light ($\lambda =$ 460 nm), it reaches the singlet excited state ([$^1FMN^{-2}$]*]) and then, by intersystem crossing, the triplet excited state ([$^3FMN^{-2}$]*]) (step 1 in Figure 2). This final excited state is a strong oxidant, which extracts two electrons from an electron donor species as NADH to provide the totally reduced [$^1FMNH^{-3}$] or [$^1FMNH_2^{-2}$] form of the flavin, depending on the pH of the solution (step 2 in Figure 2). Afterwards, the oxidative

[a] O. Azpitarte, A. Zudaire, Prof. X. Lopez, Dr. L. Salassa, Dr. E. Rezabal
Kimika Fakultatea, Euskal Herriko Unibertsitatea (UPV/EHU)
20018 Donostia, Euskadi (Spain)
E-mail: elixabete.rezabal@ehu.eus
[b] O. Azpitarte, A. Zudaire, Prof. X. Lopez, Dr. L. Salassa, Dr. E. Formoso, Dr. E. Rezabal
Donostia International Physics Center (DIPC)
20018 Donostia, Euskadi (Spain)
[c] Dr. J. Uranga
Institute for Physical Chemistry
Tammanstraße 6, 37077, Göttingen (Germany)
[d] Dr. L. Salassa
Ikerbasque, Basque Foundation for Science
48011 Bilbao, Euskadi (Spain)
[e] Dr. E. Formoso
Farmazia Fakultatea, Euskal Herriko Unibertsitatea (UPV/EHU)
01006 Gasteiz, Euskadi (Spain)

[**] A previous version of this manuscript has been deposited on a preprint server (https://chemrxiv.org/engage/chemrxiv/article-details/638da691836-ceb0ed6743584)

Supporting information for this article is available on the WWW under https://doi.org/10.1002/cphc.202300091

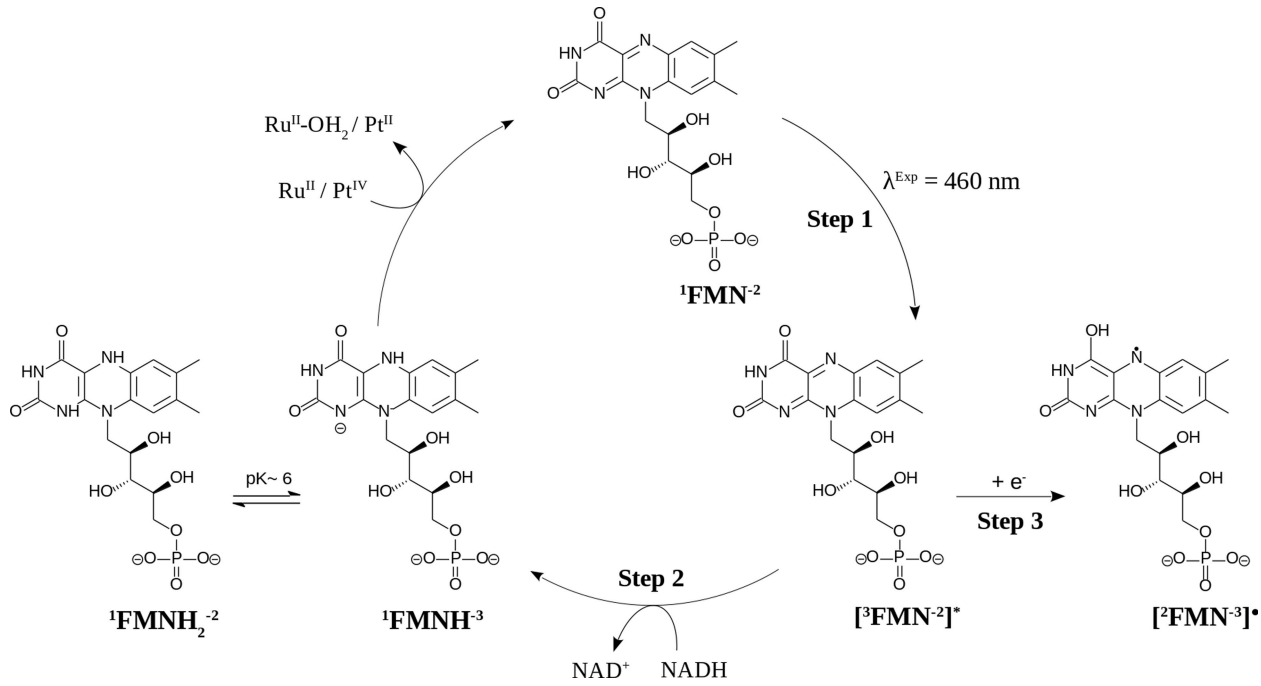

Figure 2. Catalytic mechanism of metal substrate (Pt^{IV}, Ru^{II}) photoreduction by FMN^{-2}.

half-reaction takes place, in which the reduced flavin reacts with the metal substrate (anticancer octahedral Pt^{IV} and piano-stool Ru^{II} arene complexes for example[9]), leading to their activation and reduction.[7]

As a side reaction, it has been suggested that the [^{3}FMN^{-2}]* state of the flavin can be quenched by the protein via a single electron transfer (ET), forming a semiquinone [^{2}FMN^{-3}]$^\bullet$ radical species and therefore interrupting the catalytic cycle (step 3 in Figure 2). Such an ET has previously been documented to reduce the [^{3}FMN^{-2}]* lifetime, and therefore the effectiveness of miniSOG as $^1O_2$ sensitizer.[10] On this regard, the presence of a tryptophan residue near the catalytic pocket (Trp81) has led some authors to suggest that, as happens in other flavoproteins, it is this residue that donates an electron to the flavin ring. Torra et al.,[6] in fact, observed that the mutation of the residue Trp81 into phenylalanine increases the lifetime of the triplet state (from 33.4 μs in the wild type (WT) to 1.1 ms for the W81F mutation). The glutamine in position 103 (Gln103) has also been suggested to play a crucial role in the catalytic activity, under the assumption that it enhances the electron affinity of the flavin and consequently, the ability of the protein to form a flavin radical that would quench its reactivity. In line with this theory, we observed in a previous work[8] that substituting Gln103 for a valine (mutation Q103V) increases the [^{3}FMN^{-2}]* lifetime from 35 μs in the WT miniSOG to 102 μs, also improving significantly the efficiency of Pt^{IV} prodrug reduction. Interestingly, it was also observed that the photocatalytic activity is altered by the mutation of Gln50 for a tryptophan residue (mutation Q50W), which is not in the binding pocket of the FMN, but in the entrance channel of miniSOG (see Figure S1), near to the phosphoryl group of the FMN. Upon Q50W mutation, the lifetime of [^{3}FMN^{-2}]* is reduced to 1.8 μs, the effectiveness of Pt^{IV} prodrugs reduction being also decreased significantly,[8] which was attributed to important structural alterations on the entrance channel of the miniSOG.

Nevertheless, posterior classical Molecular Dynamics (MD) simulations carried out on mutants Q50W and Q103V,[11] show that the coordination of the flavin moiety to the protein changes upon mutation, even when this takes place in a remote site. It is known that the protein environment and the interactions established with the residues in the binding pocket can tune FMN's physicochemical properties,[12] and consequently, its catalytic activity could vary upon mutation.

One of the most efficient tools to analyze these interactions throughout the different redox states and binding pockets of FMN are computational methods. In this work, we put forward a theoretical study based on Density Functional Theory (DFT) in which these physicochemical properties are studied for the different coordination modes found in the mutants analyzed. In particular, those steps assumed to be crucial in the reductive half-reaction of miniSOG, common to the various reactions the miniSOG takes part in, are analyzed: photoexcitation of the flavin (step 1 in Figure 2), double reduction of the flavin (step 2 in Figure 2), and formation of a radical on the flavin ring (step 3 in Figure 2). Additionally, the ET from Trp81 to form the radical [^{2}FMN^{-3}]$^\bullet$ species is also considered.

Computational details

The coordination of the flavin in the WT miniSOG and two mutants (Q103V and Q50W) was first addressed by means of classical

Molecular Dynamics (MD) simulations. The calculations were performed in explicit solvent using the well known AMBER99SB-ILDN force-field,[13,14] TIP3P water model[15] and periodic boundary conditions in the GROningen MAchine for Chemical Simulations (GROMACS).[16,17] The force field parameters for FMN^{-2} were obtained from previous studies through the AMBER database.[18] The crystal structure of dark-state miniSOG was obtained from Protein data Bank, PDB code 6GPU.[19]

The WT and mutated systems were solvated with water molecules in a rhombic dodecahedron box (around 8506 water molecules and a volume of 280 nm^3) and neutrality and physiologic extracellular concentration of 0.15 M was obtained by adding Na^+ and Cl^- ions at random positions.

The long-range electrostatic interactions were computed by using Particle Mesh Ewald method (PME).[20,21] Non-bonded interactions were cut at 10 Å and shifted so as to smooth the potential. All covalent bonds involving hydrogen atoms were constrained using P-LINCS algorithm[22] and 2 fs time step was used. The systems were minimized with a steepest descent algorithm followed by 2 ns canonical ensemble (NVT) equilibration using as a thermostat a velocity-rescaling scheme, known as Bussi thermostat,[23] and by another 2 ns isobaric-isothermal ensemble (NPT) equilibration using Parrinello-Rahman barostat[24] and Nose-Hoover thermostat.[25] Therefore, the equilibration of the systems was performed for 4 ns, where protein and flavin were gradually relaxed during the first 2 ns from an initial value of 5,000 $kJ\,mol^{-1}\,nm^{-2}$ of the force constant until their total free movement. Finally, 520 ns were performed for the production phase. Visual Molecular Dynamics (VMD)[26] software, GROMACS package,[16,17] MDAnalysis[27] python library and APBS software[28] were used for the visualization and analysis of the studied systems.

The complexes studied in this work were extracted from the MD trajectories and selected so that they were representative of the most relevant coordination fashion found during the simulations (see Figure 3): WT and Q103V showed a rather stable coordination and therefore, a single snapshot was carefully selected in each case, ensuring the selected snapshot agrees with the average geometrical parameters observed during the MD trajectory (see Table S8 and Figure 3 for more details). On the contrary, Q50W system showed a stable coordination throughout the trajectory in all the interactions but that around atom O2, which explored three main coordination modes during the MD simulation, and therefore, three representative snapshots were selected for Q50W (named Q50W-1, Q50W-2, and Q50W-3, c), d) and e) in Figure 3, respectively). The main difference between geometries Q50W-1, Q50W-2 and Q50W-3 is the coordination of the flavin's O2, which can take place through a direct hydrogen bond (Q50W-1) or via a water bridge, which is formed with Gln103 and Asn82 residues (Q50W-2) or only with Asn82 residue (Q50W-3).

Only the active site of the protein was selected from the MD snapshots, in order to obtaining a system size that can be studied with DFT within reasonable computational effort. The region selected for our model system includes those residues interacting directly or through a water bridge with the flavin (Gln103, Asn72, Gln44, Asn39, Arg41 and Arg57), together with Trp81 and Asn82 residues, for a better approximation to the ET process. In the first case, only the side chains of residues were included in our system. The C_α atom where truncation was done, was replaced by a methyl, Regarding Asn82 and Trp81, truncation was done at peptide bonds. The carboxylic group was replaced by a methyl group for the former and a proton was added to the amine group in the latter. The geometries of all the atoms added or modified were later optimized (B3LYP-D3/6-311+G(2d,p)) while the rest of the structure was kept frozen; the absence of imaginary modes involving the added or modified atoms was ensured by means of frequency calculations.

The suitability of this approach was assessed by performing some additional calculations on the WT, Q103V and Q50W1-3 systems. In particular, we performed hybrid quantum mechanics/molecular mechanics (QM/MM) calculations using the AMBER software package.[29] The Sander module was used for the minimization, with the QM part computed through Gaussian 16.[30] The QM region was defined to include the entire flavin moiety, a water molecule in close proximity, and the truncated residues interacting with the flavine in this geometry (Gln103, Asn72, Gln44, Asn39, Arg41, and Arg57) up to the C_β atom of their side chains.

We employed the AMBER99SB-ILDN force field and B3LYP/6-311+G(2d,p) for the minimization, including Grimme's dispersion correction. We minimized the snapshot derived from MD simulations for 250 cycles, with 50 cycles of steepest descent followed by 200 cycles of conjugate gradient. Since the system was set as non-periodic, we set the nonbonded cutoff distance to 999 Å, while any atom located more than 5.0 Å away from the QM region was restrained to its Cartesian positions using a force constant of 1000.0 $kcal\cdot mol^{-1}\cdot Å^{-2}$.

The resulting optimized geometries showed an RMSD of 0.01 Å from the respective snapshots selected from the MD trajectory (see overlap images in Figure S2), therefore supporting the suitability of our protocol for choosing a representative structure of the systems.

The following physicochemical properties were chosen for characterizing the reactivity of the flavin in each coordination site:

1. Photoexcitation of the oxidized flavin (step 1 in Figure 2). The spectrum of the singlet state is calculated by time-dependent DFT (TDDFT)[31,32] calculations, and the stability of the $[^3FMN^{-2}]$* triplet state with respect to the ground state (ΔE_{ST}) assessed.
2. Electrophylicity of the $[^3FMN^{-2}]$* state for two-electron transfer reactions (step 2 in Figure 2), thereby forming the ground state

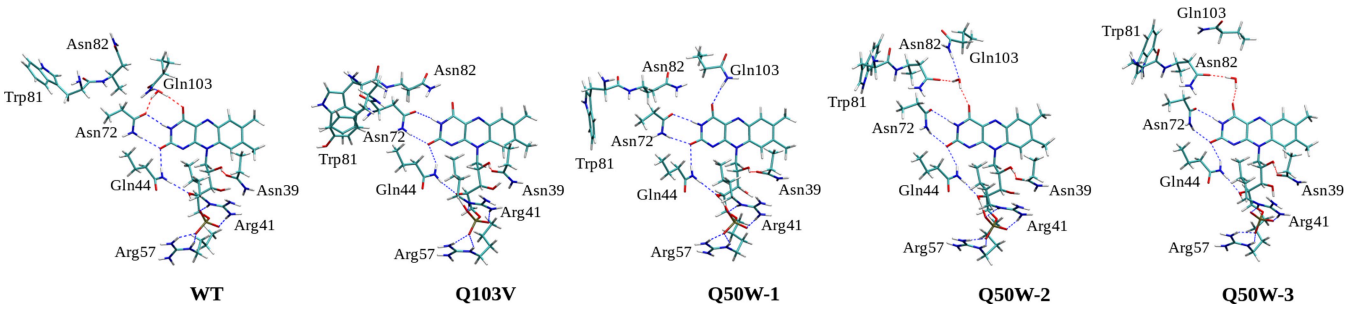

Figure 3. Coordination sites of the flavin studied in this work for the wild type miniSOG (WT), and the mutated Q103V and Q50W, geometries 1, 2 and 3.

reduced [^{1}FMNH^{-3}] species. The mechanism by which this takes place in miniSOG is still unclear, and therefore, the double reduction is estimated considering: i) an outer sphere reaction, where the two electrons are transferred to the flavin, which is later protonated (reactions 1 and 2), ii) an inner sphere reaction, where the reduction occurs via the transfer of an hydride anion[33] to the ring (reaction 2). This has been assessed by calculating the electronic energy balances (ΔE) of the following reactions:

$$^3FMN^{-2*} + 2e^- \xrightarrow{} {}^1FMN^{-4} \quad (1)$$

$$^1FMN^{-4} + H^+ \xrightarrow{} {}^1FMNH^{-3} \quad (2)$$

$$^3FMN^{-2*} + H^- \xrightarrow{} {}^1FMNH^{-3} \quad (3)$$

Finally, the double protonation of the reduced form has been considered, calculating the energy balance of the reaction 4:

$$^1FMNH^{-3} + H^+ \xrightarrow{} FMNH_2^{-2} \quad (4)$$

3. Electrophylicity of the [^{3}FMN^{-2}]* state for one-electron transfer reactions (step 3 in Figure 2), to produce the semiquinone radical. It was estimated by calculating the ΔE of the reaction 5:

$$^3FMN^{-2*} + e^- \xrightarrow{} FMN^{-3\bullet} \quad (5)$$

We would like to point out that the solvation energy of the electron and/or proton in the corresponding dielectric should be taken into account for rigorous estimation of these reaction energies. Nevertheless, this is a delicate issue for theoretical methods on one hand, and on the other, no direct experimental information is available. Therefore, we decided not to include any additional correction to these species, and we will carry out our discussion based only on relative energies (ΔΔE) with respect to a reference system (either lumiflavin (LF) or WT), to ensure error cancellation. The reactions are chosen in order to assessing the electrophylicity of the system rather than the thermochemistry of the reduction process, and therefore only the geometry of the proton and hydride atoms added in reactions 2, 3 and 4 were optimized, while the rest of the geometry was kept frozen, for the sake of consistency with the other reactions considered. Therefore, this approach does not include the posterior energy stabilization due to geometry relaxation.

Additionally, the ET from the Trp81 to [^{3}FMN^{-2}]* has been evaluated by estimating the electronic coupling between both states ($|H_{DA}|$). The process is usually described by the Marcus equation below[34] (equation 6), in which the ET rate depends on $|H_{DA}|$, the reorganization energy (λ) and the Gibbs free energy balance of the ET (ΔG). The estimation of ΔG and λ depends on the geometry variation as a result of the ET. Our model includes residues whose mobility is restrained by the protein, and therefore, the geometry variation taking place in the protein environment would not be reliably captured with such a model. Consequently, in this work we will keep the geometries fixed in the positions extracted from the protein and limit our estimation to the electronic coupling $|H_{DA}|$.

$$k_{ET} = \frac{2\pi}{\hbar}\sqrt{\frac{1}{4\pi\lambda k_B T}}|H_{DA}|^2 exp\left[\frac{-(\Delta G+\lambda)^2}{4\lambda k_B T}\right] \quad (6)$$

This was addressed by first estimating the most probable pathway from Trp81 to FMN in miniSOG and its mutants, following the Pathways model by Beratan et al.,[35] where it is assumed that the ET from the donor to the acceptor occurs via pathways, or sequences of steps from one electronic state to another. The overall penalty for ET along the pathway is then calculated as a product of penalties for each step. In particular, the Pathways 1.2 plugin for VMD was used, which permits to identify dominant ET pathways in complex systems as proteins.[36] Once the relevant residues for the ET were identified, the electron coupling was calculated at the DFT level by means of the NWChem[37] program, which follows the method of Corresponding Orbital Transformation. Convergence issues arose while performing these calculations in the model described above; therefore, considering the large dependence of the physicochemical properties of FMN on the flavin ring found throughout this work, the phosphoribityl chain was not considered when calculating the electron coupling.

DFT and in particular, B3LYP[38–40] and CAM–B3LYP[41] corrected with Grimme's dispersion correction[42] and combined with the 6-311+G(2d,p)[43–47] basis set were chosen as a good compromise between accuracy and computational efficiency. The standard free energies of reactions for the electron and proton additions to LF in gas phase were compared to previous, more thorough studies in the literature,[48] obtaining very good agreement with the levels of theory chosen in this work (see Table S1), in particular with the CAM–B3LYP functional. The protein environment was simulated by means of the Polarizable Continuum Model (PCM) using the integral equation formalism variant (IEFPCM),[49] as implemented in Gaussian16,[50] choosing different dielectric constants to simulate the protein environment at different solvent exposure degrees: ε values of 6, 20 and 78 were chosen to consider a protein buried site, a water accessible protein site, and aqueous environment, respectively. Overall, both levels of theory provided very similar results in our system; nevertheless, CAM–B3LYP has previously been observed to be a reliable choice for performing TDDFT calculations on the flavin in the miniSOG environment[12] and therefore, mainly CAM–B3LYP results are discussed throughout this manuscript, while the corresponding B3LYP data is made available (see Table S4).

Results

Influence of the protein environment

As a first assessment of our system, the influence of the phosphoribityl chain and the protein environment on the properties of the flavin ring are addressed (see Tables 1 and 2 and Figure 4 and S2, S3 and S5 for the shape of contributing orbitals in LF, FMN^{-2} and WT). This is done by comparing the data obtained for LF, FMN^{-2}, and the WT model in Figure 3.

The spectrum obtained for the LF (see black line in Figure 4 shows four main absorption peaks, which all correspond to different π-π^* transitions: HOMO-1→LUMO+1 (λ=200 nm), HOMO→LUMO+1 (λ=237 nm), HOMO-1→LUMO (λ=303 nm) and HOMO→LUMO (λ=377 nm). The lowest-lying π-π^* (HOMO→LUMO) is in our case the excitation of interest, which leads to the reactive triplet (see Figure S4), in agreement with the literature (see[12] and references therein). The relevant data for this transition is collected in Table 1.

Very similar characteristics are observed when considering the whole FMN^{-2} instead of LF, indicating that the R chain does

Table 1. Selected electronic transitions. Only those excitations with an oscillator strength (f) larger than 0.1 and contributing orbitals centered in the isoalloxazine ring, which posteriorly leads to the [^{3}FMN^{-2}]*, are presented. All electronic transition values correspond to CAM–B3LYP–D3/6-311+G(2d,p) level. The energies of donor and acceptor orbitals for each case are given in Hartrees.

Structure	Energy (eV)	λ (nm)	f	Major contribution	Donor	Acceptor
LF	3.2888	377	0.3961	HOMO→LUMO	−0.288415	−0.075476
FMN^{-2}	3.2520	381	0.3520	HOMO-3→LUMO	−0.264961	−0.053500
WT	2.6639	465	0.1735	HOMO-4→LUMO	−0.288456	−0.100218

Table 2. Electronic energy balance of the reactions considered for lumiflavin (LF), FMN^{-2} and WT. Data related to mutations is given as relative energies with respect to WT ($\Delta\Delta E$). All energies were calculated at CAM-B3LYP-D3/6-311+G(2d,p) level, choosing a dielectric constant of 6, and LF and FMN^{-2} geometries optimized at the same theory level.

				$\Delta\Delta E$ (kcal/mol)			
	LF	FMN^{-2}	WT	Q103V	Q50W-1	Q50W-2	Q50W-3
ΔE_{ST}	47.1	35.6	40.4	−0.9	6.8	3.8	3.0
ΔE_1	−162.7	−125.5	−165.7	0.4	−8.7	12.6	11.1
ΔE_2	−258.4	−269.4	−252.0	−4.5	−1.8	−8.0	−9.9
ΔE_3	−114.5	−88.4	−111.2	−4.1	−10.5	4.7	1.2
ΔE_4	−211.2	−201.4	−207.4	4.4	1.5	−2.0	−0.9
ΔE_5	−124.4	−100.1	−127.7	−0.6	−8.6	5.2	3.4

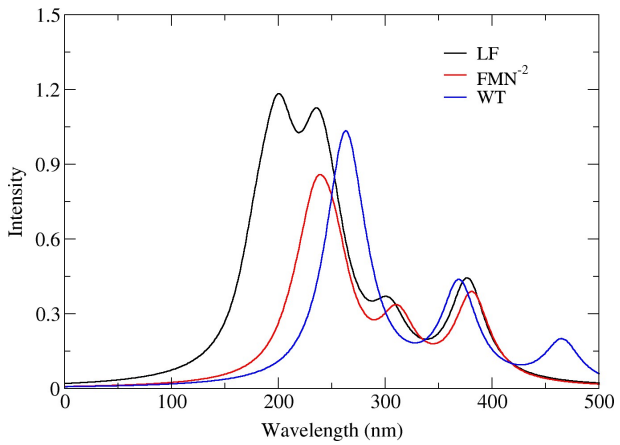

Figure 4. Theoretical spectra for LF and FMN^{-2} in free solution and WT. In all cases a dielectric constant of 6 as solvent exposure was chosen.

not influence drastically the optical properties of the ring (red spectrum in Figure 4). The maxima are found in very similar wavelengths in both cases and with very similar absorption in the case of the selected π-π^* excitation (see Table 1), which now involves the HOMO-3→LUMO orbitals (see Figure S5). When the protein environment is considered (blue line in Figure 4), the profile of the spectrum is kept, but there is a strong shift on the absorption towards higher wavelengths, in line with the literature.[12] The shift towards lower energies indicates that the presence of the protein decreases the energy difference between the involved π-π^* orbitals. In fact, it is observed that while both the donating and accepting orbitals are destabilized by about 0.02 hartrees by the presence of the phosphoribityl chain, the protein environment stabilizes back the donating orbital by the same amount, while the accepting orbital is stabilized by about 0.02 hartrees with respect to the orbitals in LF (Table 1).

Once the [^{1}FMN^{-2}]* state is reached, the triplet [^{3}FMN^{-2}]* state is formed by intersystem crossing. In this case, the insertion of the phosphoribityl chain largely stabilizes the triplet state (ΔE_{ST} in Table 2) as compared to the LF, by around 12 kcal/mol, and is slightly destabilized back by around 5 kcal/mol when the protein environment is considered. The remarkable stabilization of the triplet state in FMN^{-2} can be related to the fact that in this case the β-LUMO is centered in the phosphoryl group, in contrast to LF and WT species.

Regarding the reduction of the flavin (see Table 2), all the reactions evaluated are largely favoured, the addition of protons (ΔE_2, ΔE_4) being the process with a most negative energy balance, particularly the addition of the first proton, which is considered to be immediate after an outer sphere reduction. The double reduction ΔE_1 is more favoured than the radical formation ΔE_5, followed by the inner sphere double reduction, this is, the addition of the hydride ΔE_3. The substitution of the R chain greatly influences the results as compared to LF, less favoured reactions being predicted, overall. This is particularly the case for those reactions that imply introducing additional negative charges to the system (ΔE_1, ΔE_3, ΔE_5). The presence of the phosphoryl group forms the negatively charged FMN^{-2}, in contrast to LF, which is neutral, consequently repelling additional incoming negative charge. This is balanced when the protein environment is considered, since the negative charge of the phosphoryl is compensated by the positively charged Arg57 and Arg41 residues (see Figure 3a), obtaining results closer to the LF values. The one and two electron reductions (ΔE_1 and ΔE_5, respectively) are slightly favoured by the presence of the protein scaffold as compared to LF, due to the stabilization of the accepting orbitals in the triplet thanks to the H bonds with the residues, similar to the observed in the ground state. Those reactions implying the insertion of a H atom in the form of a hydride or proton are slightly disfavoured when the protein is

considered, which is attributed to the steric hindrance from the amino acid residues.

Influence of the mutations

Once the overall influence of the presence of a protein environment is assessed, we focus on the influence each particular coordination considered has on the reduction process. All the data regarding the WT, Q103V and Q50W systems in different dielectric environments at CAM–B3LYP and B3LYP theory levels is shown in Tables S3 and S4. The energy balances relative to WT ($\Delta\Delta E$) are presented in Table 2 for comparison.

The spectra of both WT and Q103V predict the π-π^* excitation of interest at the experimental wavelength ($\lambda =$ 465 nm vs $\lambda^{Exp} = 460$ nm), with an oscillator strength of 0.1735 and 0.2368, respectively (Table S5). The major contributing orbitals of these excitations were observed to be HOMO-4→LUMO and HOMO-5→LUMO, which correspond to HOMO→LUMO in LF (see Figure S4 and S7). Q50W structures, on the other hand, show an efficient excitation within the ring involving similar orbitals, but show a shift (between 17 and 35 nm) to minor values of λ, due to the destabilization of the HOMO-4 accepting orbital in Q50W-2 and HOMO-2 in Q50W-3 and the stabilization of the HOMO-5 in Q50W-1. Despite geometries Q50W-2-3 stabilize the LUMO as compared to LF, as seen previously, this is not as strong as in the other geometries, and furthermore, even the HOMO is slightly higher in energy in this case. On the other hand, the stabilization of the HOMO-5 in Q50W-1 can be related to its delocalization throughout the whole molecule, including the phosphoribityl chain (see Figure S7).

In line with these observations, the stability of the triplet state with respect to the ground state (ΔE_{ST} in Table 2) reflects a slightly more stable $[^3FMN^{-2}]^*$ in the case of Q103V (by about 0.9 kcal/mol), while it is destabilized by between 1.6 and 6.8 kcal/mol in the Q50W structures. These differences are mitigated as the dielectric constant increases for Q103V and Q50W-1, while it slightly increases for structures Q50W-2 and Q50W-3. This confirms the different origin of the phenomena for Q50W-1 and the rest of the Q50W geometries, which will be discussed later in the manuscript.

The relative reaction energies with respect to WT are also presented in Table 2. Only small differences between Q103V and WT results are observed; in the former, the addition of a proton (ΔE_2) and the hydride (ΔE_3) are stabilized by about −4 kcal/mol as compared to WT, and the second protonation (ΔE_4) is destabilized by the same amount, the rest of the deviations being smaller than 1 kcal/mol. While these energy differences lie around the expected accuracy of DFT, significant differences are found in Q50W structures. Most remarkably, the double reduction (ΔE_1) becomes less favoured by about 10–13 kcal/mol, excepting Q50W-1, for which the reduction energy decreases significantly, by −8.7 kcal/mol. The hydride transfer and the single electron reduction are disfavoured in geometries Q50W-2 and Q50W-3 by between 1.2 kcal/mol and 5.2 kcal/mol, while are largely favoured in geometry Q50W-1 (−10.5 kcal/mol and −8.6 kcal/mol, respectively). The origin is probably on the different spin distribution of complex Q50W-1, where the spin density around the ring is lower (1.56 vs 2.01–2.02 for the rest of the complexes, see Table S6) which allows the flavin to receive additional negative charge with less repulsion than any other structure. In particular, this spin distribution is related to the delocalized β-LUMO of the $[^3FMN^{-2}]^*$ (already observed in the ground state singlet HOMO-5), while it is not observed for the β-LUMO + 1. Consequently, all reduction reactions (ΔE_1, ΔE_3, ΔE_5) show similar stabilizations in this case. The delocalization of the spin towards the ribityl chain is more remarked as we consider higher dielectrics (see Table S6), which should in principle lead to even lower reduction energies. Nevertheless, this is not the case, since as the dielectric increases, the difference with respect to WT becomes negligible, pointing out to a more efficient screening of the negative charges in higher dielectrics that attenuate the repulsion. It is interesting to observe that while the tendencies are kept for Q50W-2 and Q50W-3 when B3LYP is chosen, Q50W-1 shows no significant difference from the WT geometry in any of the reactions considered.

In fact, the single reduction reaction energy could be satisfactorily related to the triplet β-LUMO orbital energy the incoming electron occupies (see Figure 5 and Figure S8). A similar tendency was observed also for the double reduction; the energy difference between the double and the single reductions could be related to the radical β-LUMO (see Figure S10, and S11), indicating that both reductions are ultimately modulated by the stability of the accepting orbitals.

On the contrary, the first protonation becomes significantly more favoured in all the structures with respect to the WT, with an increase (in absolute values) between 2 and 10 kcal/mol. Again, the most significant differences are observed in the Q50W-2 and Q50W-3 structures. The second protonation, instead, is overall very similar in all the complexes.

Finally, it is interesting to observe that the hydride insertion shows a similar behaviour as the single reduction reaction. This is likely due to the same formal charge (−1) in both cases, and

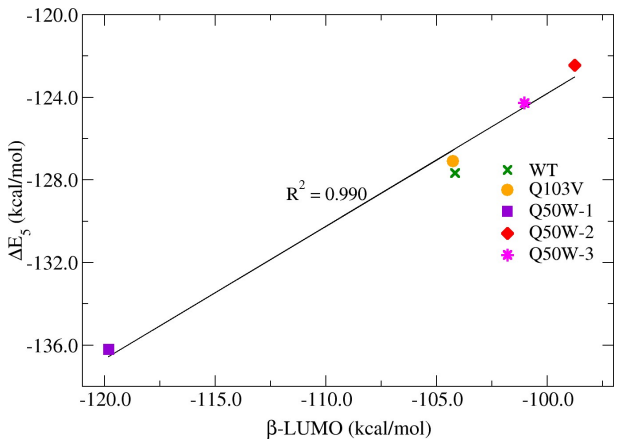

Figure 5. Radical formation energy (ΔE_5) as a function of β-LUMO in $[^3FMN^{-2}]^*$ for the studied geometries. All energies were calculated at CAM-B3LYP-D3/6-311 + G(2d,p) level, within a dielectric environment of 6.

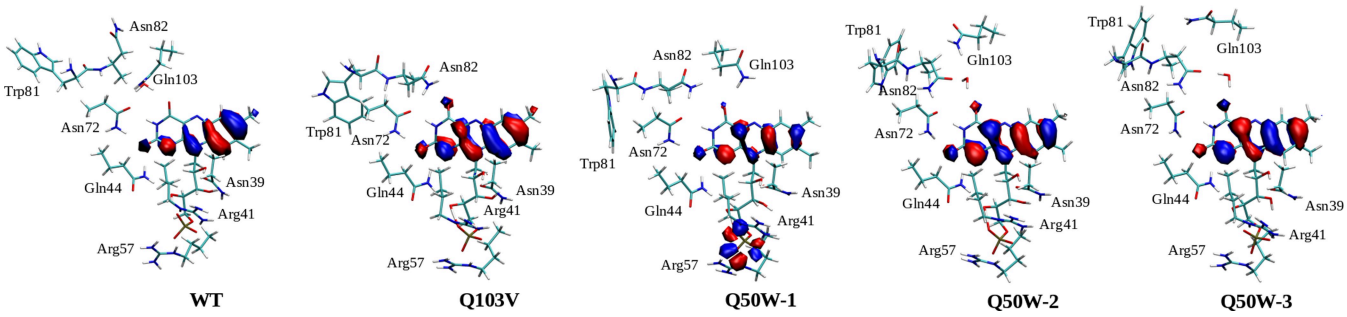

Figure 6. β-LUMO orbitals in [^{3}FMN^{-2}]* for WT, Q103V and Q50W-1-3. All orbitals were calculated at CAM-B3LYP-D3/6-311 + G(2d,p) level, within a dielectric environment of 6.

therefore, similar electrostatic repulsion on one hand, and the balance between the opposite reduction and protonation tendencies that mitigate the total influence of the hydride insertion as compared to the double reduction. Nevertheless, both ΔE_3 and ΔE_5 showing a similar behaviour implies no change in the reactivity, which indicates a more relevant role of the outer sphere reduction in this reactivity.

Electron transfer

In this section, we estimate the radical formation due to the ET from the residue Trp81 to flavin by analyzing the $|H_{DA}|$ of such a process. The most relevant pathways found for the different structures reveal that the asparagine residues around the flavin play a fundamental role in the ET from Trp81 to the isoalloxazine ring (see Table 3). In particular, residue Asn72 enables the ET in the WT geometry, while in the Q103V mutation residues Asn82 and Asn72 are the ones participating. Finally, the ET takes place through the residue Asn82 in the Q50W mutation, with variable participation of solvent molecules depending on the particular geometry observed.

Our models, even if they are small, contain all the atoms participating in the paths identified by Baratan's model as the most likely pathways for an ET from Trp81 to FMN^{-2}. $|H_{DA}|$ was estimated by means of constrained DFT (cDFT) calculations, in which initially the unpaired electrons are located in the flavin ring, and the Trp81 has a closed shell electronic structure. After the ET, one of the unpaired electrons is on the Trp81 ring and the other one in the flavin ring (see the Figure S12 for more details). A word of caution should be issued at this stage with respect to the Q50W-1 structure: the model used for calculating the couplings does not include the phosphoribityl chain, and therefore the spin is initially located on the ring, which would not be the case if the whole model was considered. Consequently, this data will not be included in the discussion.

Table 3. Electronic couplings ($|H_{DA}|$), in cm^{-1}, together with the residues involved in the Trp81-FMN pathway in each case.

Mutation	Path	$\lvert H_{DA}\rvert$
WT	Asn72	42
Q103V	Asn82, Asn72	10
Q50W-1	Asn82	19
Q50W-2	Asn82, water	5
Q50W-3	Asn82, water	187

The $|H_{DA}|$ values obtained for each case are presented in Table 3. The coupling is smaller in Q103V than in WT, suggesting a less efficient ET. The couplings for the Q50W geometries lie within a wide range of values, from 5 to 187 cm^{-1}. The highest coupling is achieved in the Q50W-3 geometry, with a value one order of magnitude larger than that of WT. This structure is characterized for being the only one among the Q50W structures where the predicted path is hydrogen bonded and no other interaction is established with other residues, consequently optimizing the coupling between the initial and final electronic states of the ET. Although a strong electronic coupling only does not ensure the ET process, it does suggest that in this case the ET could take place more easily in Q50W mutation than in any other mutation studied, in line with the experimental results indicating a stronger quenching in this protein.[8]

Discussion

As expected, we observe that the protein environment does influence the redox and optical properties of the FMN^{-2}; it is observed that the π-π^* transition is red shifted in the different miniSOG environments considered as compared to the gas phase, due to the H-bond interactions with the protein scaffolds.[12] This responds to the rather homogeneous net of H bonds formed by the different protein scaffolds with the flavin, in terms of the flavin atoms interacting (O1, O2 and H1) and the charge of the residues establishing such interactions (neutral). More specifically, the coordination in the different mutants varies only in the O2 position of the isoalloxazine unit. Nevertheless, this difference is enough to result in significant reactivity and ET differences between the mutants.

The environments identified for O2 in the different structures considered are: no interactions (Q103V), direct interaction with Gln103 (Q50W-1) or water. Besides, the latter can be simultaneously interacting with Gln103 (WT), Asn82 (Q50W-3), or both (Q50W-2). It had been previously suggested

in the literature that Gln103 could be fundamental for describing the catalytic activity of miniSOG, but in this work we find that additional factors may also be involved. Several works in the literature mention the relevant role of interactions with N3 in the stabilization of the semiquinone and in flavin's thermochemistry.[51] This influence is related to the fact that the negative charge of this atom increases significantly when the ET to the flavin takes place.[52] Consequently, its interaction with protein residues is expected to change the stability of the semiquinone and therefore, the electron affinity of the FMN in a certain protein environment. Probably, the assumption that Gln103 plays a fundamental role in miniSOG's chemistry arises from its vicinity to this binding site. Nevertheless, in our works[11] (and others in the literature[6,12]) we have observed that Gln103 does not interact with N3 in miniSOG, but with O2, and therefore its influence is not as determinant as expected.

This becomes apparent if the reduction reaction energies of Gln103 and WT are compared: even if Gln103 is absent in Q103V, the energy balances studied are very similar to those of WT. The most relevant alteration of properties is observed for Q50W, which deviates significantly from the other miniSOG structures. These deviations can be separated in those regarding Q50W-1, and the ones corresponding to Q50W-2-3.

Q50W-1 triplet shows significantly favoured reductions, double (ΔE_1, ΔE_3) or single (ΔE_5), by around 8.5–10.5 kcal/mol. This has been related to the delocalization of the accepting orbital towards the phosphoryl, which diminishes the repulsion towards the incoming charge and stabilizes the orbital. As the dielectric considered increases and the flavin becomes more exposed to water, this deviation is attenuated, due to the charge screening. Consequently, despite the direct interaction with Gln103, the enhanced electrophylicity in Q50W-1 is equally observed in one and two electron reductions, and therefore does not point out to a more efficient quenching by the protein.

On the contrary, the reduction reactions are disfavoured in Q50W-2-3; furthermore, this is specially remarked in the double reduction ΔE_1 (10–13 kcal/mol), as compared to 1–7 kcal/mol for ΔE_3 and ΔE_5. In these structures, the insertion of a water molecule permits Asn82 to establish a water-bridged coordination with the isoalloxazine ring, and consequently the water bridged coordination with Gln103 is loosened (2.260 Å in Q50W-2) or lost (Q50W-3) as compared to that on the WT geometry (1.894 Å, see Table S8 for a deep analysis), which might not be as strongly stabilizing as other coordination patterns (see Figure 3). Remarkably, even though structures Q50W-2-3 diverge in the interaction this water establishes with the Asn82 (1.660 Å and 1.725 Å, respectively), they show very similar tendencies, which could mean that Asn82 primarily modulates the electron transfer process and not the electron affinity. This is not observed in WT, since Asn82 presents another orientation and does not interact with the water molecule. Therefore, both the presence of the water interacting with the flavin and the elongation or absence of the Gln103 residue are in the origin of this effect, which is overall related to the destabilization of the accepting orbitals, and does not vary significantly with the solvent exposure degree. This would indicate that, as compared to WT, the competition between a double reduction and a single reduction remains unaltered in the case of Q103V and Q50W-1, while the Q50W-2-3 mutation would be less prone to the double reduction as compared to the single reduction.

These trends in the reduction process are governed by the frontier orbitals of each structure. The stability of the electron accepting orbitals modulates the electron affinity, namely the β-LUMO and β-LUMO+1 of the triplet, which are HOMO-LUMO in the ground state, and β-HOMO and β-LUMO in the radical, respectively. The most relevant tendencies observed are (1) the delocalization and consequent stabilization of the $^1FMN^{-2}$ HOMO in Q50W-1, which leads to a higher ΔE_{ST}, and favoured reduction ($\Delta E_1 = -8.7$ kca/mol, $\Delta E_3 = -10.5$ kca/mol, $\Delta E_5 = -8.6$ kca/mol) and (2) the destabilization of the $^1FMN^{-2}$ HOMO and specially LUMO in Q50W-2-3, which results on the diminished electroaffinity on both one and two electron reductions, the former being specially intense ($k\Delta E_1 = 12.6$–10.5 kca/mol, $\Delta E_3 = 1.2$–6.7 kca/mol, $\Delta E_5 = 3.4$–5.2 kca/mol). This seems to be related to the water bridge with Asn82 present in these structures, which is absent in the rest of moieties. Regarding Q103V, the variations are small and therefore, the energy balance is similar.

Finally, additional insight is obtained from the ET $|H_{DA}|$ values. The coupling is predicted to be lowest in Q103V, followed by WT and quite variable in the Q50W geometries. Anyhow, the Q50W-3 is predicted to have a coupling at least an order of magnitude larger than any other geometry, indicating a very efficient radical formation when that particular geometry is explored (150 ns from a total of 520 ns). Q103V, instead, shows a lower electronic coupling than WT, pointing out to a less efficient ET that could be on the origin of the improved catalytic performance observed experimentally.

Conclusion

In this work, the analysis of our model has permitted to rationalize the experimental results previously obtained regarding the catalytic activity of the miniSOG and its mutants towards the conversion of metal-based prodrug precursors. The catalytic activity of the miniSOG is based on a redox reaction in which initially the flavin is reduced and posteriorly oxidated. We have focused our attention on the reductive half-reaction, observing that it can be significantly altered by the residues coordinated to FMN. More specifically, the evaluation of selected reaction energies has enabled us to trace back the reactivity of the flavin to the electroaffinity and $|H_{DA}|$ differences of the various coordination modes considered. It is remarkable that the coordination modes mainly differ only on the interactions established by the O2 atom of the flavin.

In particular, Q50W mutation overall disfavours the double reduction as compared to the single electron transfer, therefore facilitating the quenching, which is further enhanced by the efficient electronic coupling for the ET. This is ultimately related to the destabilization of the LUMO orbital of the flavin ground state in the presence of the O2-water-Asn82 moiety.

On the other hand, Q103V mutation does not remarkably influence the single/double reduction balance as compared to the native miniSOG, but the electronic coupling does indicate a less probable ET, leading to a more efficient catalyst.

This study focuses on the reductive half-reactivity of miniSOG, and therefore, other factors as the accessibility of the flavin[8] or the oxidative half-reaction, potentially relevant in explaining miniSOG catalytic activity alteration upon mutations, are not considered. Nevertheless, the important electroaffinity and $|H_{DA}|$ differences observed in this part of the reaction explain the main lines of the experimental results previously obtained regarding the influence of the mutations, indicating that the reductive half-reaction might be a determining part of the whole catalytic cycle.

Acknowledgements

We acknowledge the Basque Government – Eusko Jaurlaritza (IT1254-19, IT1584-22, IkasC-2021-1-0252 (A.Z.), PIBA_2021_1_0034 (L.S.)), University of the Basque Country UPV/EHU (PIF19/244), Spanish State Research Agency (PID2019-109111RB-I00 (L.S., E.R. O.A.), PGC2018-097529-B-100 (X.L., E.F.), and FPU20/00688 (O.A.)) and Diputación Foral de Gipuzkoa (RED 2021) for financial support and the SGi/IZO-SGIker UPV/EHU for generous allocation of computational resources. Prof. Jesus Ugalde is acknowledged for fruitful discussions about electron transfer processes. L.S. thanks the Spanish Multi-MetDrugs RED2018-102471-T. This work was performed under the Severo Ochoa Centres of Excellence Programme run by the Spanish State Research Agency, CEX2018-000867-S (DIPC).

Conflict of Interests

The authors declare no conflict of interest.

Data Availability Statement

The data that support the findings of this study are available in the supplementary material of this article.

Keywords: Electron transfer · Flavoprotein · DFT · Redox reactions · Catalysis

[1] M. W. Fraaije, A. Mattevi, *Trends Biochem. Sci.* **2000**, *25*, 126.
[2] A. Losi, *Photochem. Photobiol.* **2007**, *83*, 1283.
[3] R. Miura, *Chem. Rec.* **2001**, *1*, 183.
[4] X. Shu, V. Lev-Ram, T. J. Deerinck, Y. Qi, E. B. Ramko, M. W. Davidson, Y. Jin, M. H. Ellisman, R. Y. Tsien, *PLoS Biol.* **2011**, *9*, 1.
[5] R. Ruiz-González, A. L. Cortajarena, S. H. Mejias, M. Agut, S. Nonell, C. Flors, *J. Am. Chem. Soc.* **2013**, *135*, 9564.
[6] J. Torra, C. Lafaye, L. Signor, S. Aumonier, C. Flors, X. Shu, S. Nonell, G. Gotthard, A. Royant, *Sci. Rep.* **2019**, *9*, 1.
[7] J. Gurruchaga-Pereda, V. Martínez-Martínez, E. Rezabal, X. Lopez, C. Garino, F. Mancin, A. Cortajarena, L. Salassa, *ACS Catal.* **2020**, *10*, 187.
[8] J. Gurruchaga-Pereda, V. Martínez-Martínez, E. Formoso, O. Azpitarte, E. Rezabal, X. Lopez, A. L. Cortajarena, L. Salassa, *J. Phys. Chem. Lett.* **2021**, *12*, 4504.
[9] S. Alonso-de Castro, A. L. Cortajarena, F. López-Gallego, L. Salassa, *Angew. Chem. Int. Ed.* **2018**, *57*, 3143.
[10] M. Westberg, L. Holmegaard, F. M. Pimenta, M. Etzerodt, P. R. Ogilby, *J. Am. Chem. Soc.* **2015**, *137*, 1632.
[11] O. Azpitarte, X. Lopez, L. Salassa, E. Rezabal, E. Formoso, *To be published* **2023**.
[12] N. H. List, F. M. Pimenta, L. Holmegaard, R. L. Jensen, M. Etzerodt, T. Schwabe, J. Kongsted, P. R. Ogilby, O. Christiansen, *Phys. Chem. Chem. Phys.* **2014**, *16*, 9950.
[13] K. Lindorff-Larsen, S. Piana, K. Palmo, P. Maragakis, J. Klepeis, R. Dror, D. Shaw, *Proteins* **2010**, *78*, 1950.
[14] M. Robertson, J. Tirado-Rives, W. Jorgensen, *J. Phys. Chem. Lett.* **2016**, *7*, 3032.
[15] W. Jorgensen, J. Chandrasekhar, J. Madura, R. Impey, M. Klein, *J. Chem. Phys.* **1983**, *79*, 926.
[16] M. J. Abraham, T. Murtola, R. Schulz, S. Páll, J. C. Smith, B. Hess, E. Lindahl, *SoftwareX* **2015**, *1–2*, 19.
[17] S. Páll, M. J. Abraham, C. Kutzner, B. Hess, E. Lindahl, *Solving Software Challenges for Exascale* **2015**, page 3–27.
[18] C. Schneider, J. Sühnel, *Biopolymers* **1999**, *50*, 287.
[19] J. Torra, C. Lafaye, L. Signor, S. Aumonier, C. Flors, X. Shu, S. Nonell, G. Gotthard, A. Royant, *Sci. Rep.* **2019**, *9*, 2428.
[20] T. Darden, D. M. York, L. Pedersen, *J. Chem. Phys.* **1993**, *98*, 10089.
[21] U. Essmann, L. Perera, M. L. Berkowitz, T. Darden, H. Lee, L. G. Pedersen, *J. Chem. Phys.* **1995**, *103*, 8577.
[22] B. Hess, *J. Chem. Theory Comput.* **2008**, *4*, 116.
[23] G. Bussi, D. Donadio, M. Parrinello, *J. Chem. Phys.* **2007**, *126*, 014101.
[24] M. Parrinello, A. Rahman, *J. Appl. Phys.* **1981**, *52*, 7182.
[25] S. Nosé, *Mol. Phys.* **1984**, *52*, 255.
[26] W. Humphrey, A. Dalke, K. Schulten, *J. Mol. Graphics* **1996**, *14*, 33.
[27] M. Khoshlessan, I. Paraskevakos, S. Jha, O. Beckstein, Parallel Analysis in MDAnalysis using the Dask Parallel Computing Library, in *Proceedings of the 16th Python in Science Conference*, SciPy, pages 64–72.
[28] E. Jurrus, D. Engel, K. Star, K. Monson, J. Brandi, L. E. Felberg, D. H. Brookes, L. Wilson, J. Chen, K. Liles, M. Chun, P. Li, D. W. Gohara, T. Dolinsky, R. Konecny, D. R. Koes, J. E. Nielsen, T. Head-Gordon, W. Geng, R. Krasny, G.-W. Wei, M. J. Holst, J. A. McCammon, N. A. Baker, *Protein Sci.* **2017**, *27*, 112.
[29] D. Case, K. Belfon, I. Ben-Shalom, S. Brozell, D. Cerutti, T. Cheatham III, V. Cruzeiro, T. Darden, R. Duke, G. Giambasu, M. Gilson, H. Gohlke, A. G. R. Harris, S. Izadi, S. Izmailov, K. Kasavajhala, A. Kovalenko, R. Krasny, T. Kurtzman, T. Lee, S. LeGrand, P. Li, C. Lin, J. Liu, T. Luchko, R. Luo, V. Man, K. Merz, Y. Miao, O. Mikhailovskii, G. Monard, H. Nguyen, A. Onufriev, F. Pan, S. Pantano, R. Qi, D. Roe, A. Roitberg, C. Sagui, S. Schott-Verdugo, J. Shen, C. Simmerling, N. Skrynnikov, J. Smith, J. Swails, R. Walker, J. Wang, L. Wilson, R. Wolf, X. Wu, Y. Xiong, Y. Xue, D. York, P. Kollman, *AMBER*, University of California, San Francisco, **2020**.
[30] A. W. Götz, M. A. Clark, R. C. Walker, *J. Comb. Chem.* **2014**, *35*, 95.
[31] F. Furche, R. Ahlrichs, *J. Chem. Phys.* **2002**, *117*, 7433.
[32] G. Scalmani, M. J. Frisch, B. Mennucci, J. Tomasi, R. Cammi, V. Barone, *J. Chem. Phys.* **2006**, *124*, 94107.
[33] S. Scoditti, E. Dabbish, E. Sicilia, *J. Inorg. Biochem.* **2021**, *219*, 111447.
[34] R. A. Marcus, N. Sutin, *Biochim. Biophys. Acta Rev. Bioenerg.* **1985**, *811*, 265.
[35] D. N. Beratan, J. N. Betts, J. N. Onuchic, *Science* **1991**, *252*, 1285.
[36] I. A. Balabin, X. Hu, D. N. Beratan, *J. Comput. Chem.* **2012**, *33*, 906.
[37] E. Aprà, E. J. Bylaska, W. A. de Jong, N. Govind, K. Kowalski, T. P. Straatsma, M. Valiev, H. J. J. van Dam, Y. Alexeev, J. Anchell, V. Anisimov, F. W. Aquino, R. Atta-Fynn, J. Autschbach, N. P. Bauman, J. C. Becca, D. E. Bernholdt, K. Bhaskaran-Nair, S. Bogatko, P. Borowski, J. Boschen, J. Brabec, A. Bruner, E. Cauët, Y. Chen, G. N. Chuev, C. J. Cramer, J. Daily, M. J. O. Deegan, T. H. Dunning, M. Dupuis, K. G. Dyall, G. I. Fann, S. A. Fischer, A. Fonari, H. Früchtl, L. Gagliardi, J. Garza, N. Gawande, S. Ghosh, K. Glaesemann, A. W. Götz, J. Hammond, V. Helms, E. D. Hermes, K. Hirao, S. Hirata, M. Jacquelin, L. Jensen, B. G. Johnson, H. Jónsson, R. A. Kendall, M. Klemm, R. Kobayashi, V. Konkov, S. Krishnamoorthy, M. Krishnan, Z. Lin, R. D. Lins, R. J. Littlefield, A. J. Logsdail, K. Lopata, W. Ma, A. V. Marenich, J. del Campo, D. Mejia-Rodriguez, J. E. Moore, J. M. Mullin, T. Nakajima, D. R. Nascimento, J. A. Nichols, P. J. Nichols, J. Nieplocha, A. Otero-de-la Roza, B. Palmer, A. Panyala, T. Pirojsirikul, B. Peng, R. Peverati, J. Pittner, L. Pollack, R. M. Richard, P. Sadayappan, G. C. Schatz, W. A. Shelton, D. W. Silverstein, D. M. A. Smith, T. A. Soares,

D. Song, M. Swart, H. L. Taylor, G. S. Thomas, V. Tipparaju, D. G. Truhlar, K. Tsemekhman, T. Van Voorhis, Á. Vázquez-Mayagoitia, P. Verma, O. Villa, A. Vishnu, K. D. Vogiatzis, D. Wang, J. H. Weare, M. J. Williamson, T. L. Windus, K. Woliński, A. T. Wong, Q. Wu, C. Yang, Q. Yu, M. Zacharias, Z. Zhang, Y. Zhao, R. J. Harrison, *J. Chem. Phys.* **2020**, *152*, 184102.
[38] A. D. Becke, *Phys. Rev. A* **1988**, *38*, 3098.
[39] C. Lee, W. Yang, R. G. Parr, *Phys. Rev. B* **1988**, *37*.
[40] P. J. Stephens, F. J. Devlin, C. F. Chabalowski, M. J. Frisch, *J. Phys. Chem.* **1994**, *98*, 11623.
[41] T. Yanai, D. P. Tew, N. C. Handy, *Chem. Phys. Lett.* **2004**, *393*, 51.
[42] S. Grimme, J. Antony, S. Ehrlich, H. Krieg, *J. Chem. Phys.* **2010**, *132*, 154104.
[43] B. P. Pritchard, D. Altarawy, B. Didier, T. D. Gibsom, T. L. Windus, *J. Chem. Inf. Model.* **2019**, *59*, 4814.
[44] D. Feller, *J. Comput. Chem.* **1996**, *17*, 1571.
[45] K. L. Schuchardt, B. T. Didier, T. Elsethagen, L. Sun, V. Gurumoorthi, J. Chase, J. Li, T. L. Windus, *J. Chem. Inf. Model.* **2007**, *47*, 1045.
[46] T. Clark, J. Chandrasekhar, G. W. Spitznagel, P. V. R. Schleyer, *J. Comput. Chem.* **1983**, *4*, 294.
[47] R. Krishnan, J. S. Binkley, R. Seeger, J. A. Pople, *J. Chem. Phys.* **1980**, *72*, 650.
[48] S. Bhattacharyya, M. T. Stankovich, D. G. Truhlar, J. Gao, *J. Phys. Chem. A* **2007**, *111*, 5729.
[49] G. Scalmani, M. J. Frisch, *J. Chem. Phys.* **2010**, *132*, 114110.
[50] M. J. Frisch, G. W. Trucks, H. B. Schlegel, G. E. Scuseria, M. A. Robb, J. R. Cheeseman, G. Scalmani, V. Barone, B. Mennucci, G. A. Petersson, H. Nakatsuji, M. Caricato, X. Li, H. P. Hratchian, A. F. Izmaylov, J. Bloino, G. Zheng, J. L. Sonnenberg, M. Hada, M. Ehara, K. Toyota, R. Fukuda, J. Hasegawa, M. Ishida, T. Nakajima, Y. Honda, O. Kitao, H. Nakai, T. Vreven, J. A. Montgomery Jr, J. E. Peralta, F. Ogliaro, M. Bearpark, J. J. Heyd, E. Brothers, K. N. Kudin, V. N. Staroverov, R. Kobayashi, J. Normand, K. Raghavachari, A. Rendell, J. C. Burant, S. S. Iyengar, J. Tomasi, M. Cossi, N. Rega, J. M. Millam, M. Klene, J. E. Knox, J. B. Cross, V. Bakken, C. Adamo, J. Jaramillo, R. Gomperts, R. E. Stratmann, O. Yazyev, A. J. Austin, R. Cammi, C. Pomelli, J. W. Ochterski, R. L. Martin, K. Morokuma, V. G. Zakrzewski, G. A. Voth, P. Salvador, J. J. Dannenberg, S. Dapprich, A. D. Daniels, Ö. Farkas, J. B. Foresman, J. V. Ortiz, J. Cioslowski, D. J. Fox, *Gaussian16 Revision A.03*.
[51] K. Y. Yang, R. P. Swenson, *Biochem.* **2007**, *46*, 2289.
[52] I. Nogués, L. A. Campos, J. Sancho, C. Gómez-Moreno, S. G. Mayhew, M. Medina, *Biochem.* **2004**, *43*, 15111.

Manuscript received: February 3, 2023
Revised manuscript received: May 12, 2023
Accepted manuscript online: May 16, 2023
Version of record online: May 16, 2023